AERODYNAMIC HEATING AT HYPERSONIC SPEEDS

Humberto Araujo Machado, humbertoam@iae.cta.br
José Bezerra Pessoa Filho, bezerra@iae.cta.br
Instituto de Aeronáutica e Espaço – IAE
Comando-Geral de Tecnologia Aeroespacial - CTA
Pr. Mal. Eduardo Gomes, 50, Vila das Acácias
12228-904
São José dos Campos, SP

Abstract. *Aerodynamic heating on a sounding rocket flying at hypersonic speed is evaluated. The fluid flow properties are obtained in an approximated fashion, whereas the convective heat flux is calculated from classical relationships provided in the literature to this type of problem. Since an ablative type of material is applied as thermal protection system at some locations, a transient one-dimensional coupled conductive-change phase material problem results. The finite volume method is then used to solve the resulting equations and temperature distributions are obtained at the most critical regions of the rocket. For one of the simulations, it was possible to compare the obtained results against experimental measurements, taken during the flight of a VSB-30 sounding rocket.*

Keywords*: Aerodynamic heating, Sounding rocket, Heat transfer, Phase change material*

1. INTRODUCTION

Sounding rockets are extensively used to study the upper layers of the earth's atmosphere and to provide microgravity environments. The Institute of Aeronautics and Space (IAE) has designed, built and launched hundreds of sounding rockets along the past 40 years. Some of them are developed upon request of other countries. This is the case of VSB-30, a two-stage sounding rocket developed for use by DLR (German Space Agency). Figure 1 shows a schematic representation of VSB-30. It has a total length of *13 m* and a diameter of *0,6 m*. It is equipped with two solid propellant motors, namely S31 and S30. S31 acts like a booster during its *15 s* burning time, whereas S30 burns for about *30 s*, reaching a maximum altitude of 28*0 km* approximately. During its flight VSB-30 provides *6 minutes* of microgravity environment.

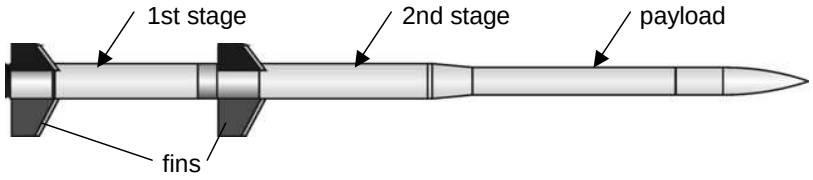

Figure 1. VSB-30 sounding rocket.

Figure 2 shows altitude and velocity maps for VSB-30 (Garcia, 2003). It reaches the speed of *6.500 km/h* while still flying within the earth's atmosphere. For practical purposes continuous flow regime is assumed to exist for altitudes below *90 km*. Beyond *90 km*, vacuum is assumed.

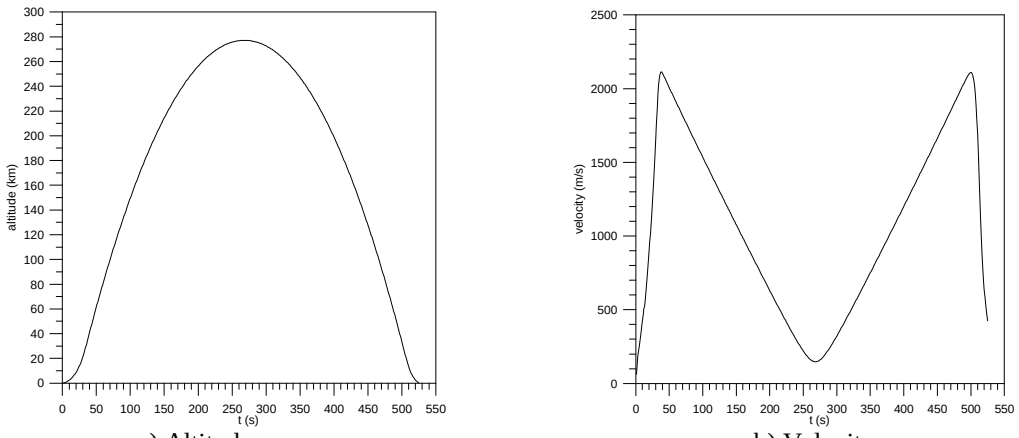

a) Altitude map b) Velocity map

Figure 2. Trajectory of VSB-30.

As a result of its very high speeds, aerodynamic heating arises as a major problem in the VSB-30 design. This problem is larger near the stagnation regions, such as those existing at the nose cap, the payload and the fins´ leading edges. Due to the air compression, caused by strong normal shocks near these regions, air temperature surpasses *2100 °C*. As a consequence, heat is transferred to VSB-30 surface. Since such surfaces are mostly made of metals, it is mandatory to evaluate their temperature levels specifying, if necessary, an adequate thermal protection system. This development is an improved version of a previous work (Mazzoni et al., 2005).

2. FORMULATION

2.1 Inviscid flow conditions

To predict the heat transfer to VSB-30, it is necessary to know pressure, temperature and velocity fields around the rocket. That can be accomplished by numerically solving the boundary layer equations. However, such a procedure is expensive and time consuming. In the present work a simpler, but reliable, engineering approach is used. The following simplifying assumptions are made:

- Zero angle of attack;
- VSB-30 rotation around its longitudinal axis is neglected;
- Atmospheric air is considered to behave as a calorically and thermally perfect gas (no chemical reactions); and
- Wall heating is only by convection, and conduction occurs only in the direction normal to the surface.

The free stream conditions ahead of the fins and nose cap are those given by v_∞, T_∞, p_∞, corresponding, respectively, to velocity, temperature and pressure. By knowing v_∞ and altitude, as a function of time, together with an atmospheric model (US Standard Atmosphere, 1976), it is possible to evaluate the free stream properties, such as p_∞, T_∞ and c_∞, which represent free stream pressure, temperature and speed of sound, respectively. For supersonic flow ($M_\infty > 1$), which begins at *8 s* (altitude of *2 km*), a detached bow shock wave appears ahead of the nose and fins, Fig. 3. By using the normal shock relationships (Anderson Jr., 1989), it is possible to calculate v_1, T_1 and p_1 after the shock.

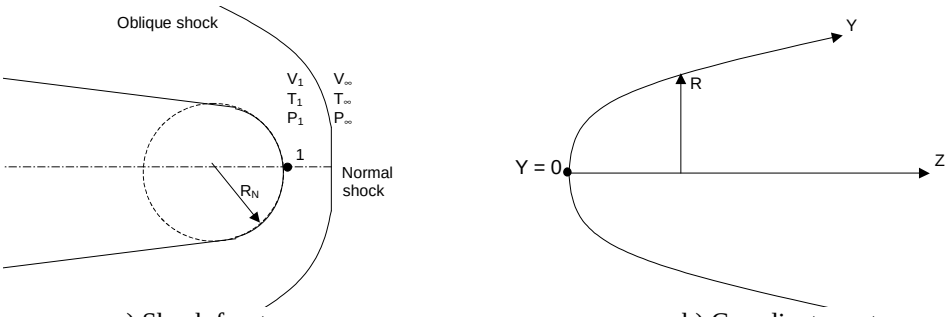

a) Shock front b) Coordinate system

Figure 3. Schematic representation of shock front and coordinate system.

2.2 Convective heat transfer to the surfaces

The heat flux over the external surface was calculated through the Zoby's method (Zoby et al., 1981; Miranda and Mayal, 2001), namely:

$$q = h(T_{aw} - T_w) \tag{1}$$

where q is the heat flux, T_w is the wall temperature and T_{aw} is the adiabatic wall temperature, given by:

$$T_{aw} = T_e + F_R \frac{v_e^2}{2c_p} \tag{2}$$

where c_p is the specific heat, T_e the temperature and v_e the velocity. The subscript *e* refers to conditions at the boundary layer edge. F_R is the recovery factor, equal to $\sqrt{Pr_w}$ for laminar flow and $\sqrt[3]{Pr_w}$ for turbulent flow. Pr_w is the Prandtl number evaluated at wall temperature, $Pr_w \approx 0.71$. The convective heat transfer coefficient comes from the Reynolds analogy, namely:

$$h = 0.5\rho_e c_p v_e \, \mathrm{Pr}_w^{-a} \, C_F \tag{3}$$

where a is equal to *0.6* and *0.4* for laminar and turbulent flow, respectively. To take into account compressibility effects, a modified friction factor is obtained (Anderson, 1990):

$$C_F = K_1 (Re_\theta)^{K_2} \left(\frac{\rho_e^*}{\rho_e}\right)\left(\frac{\mu_e^*}{\mu_e}\right)^{K_3} \tag{4}$$

In the equation above, Re_θ is the Reynolds number, based on the boundary layer thickness, θ:

$$Re_\theta = \frac{\rho_e V_e \theta}{\mu_e} \tag{5}$$

The superscript "*" refers to properties evaluated at Eckert's reference temperature (T_e*). Viscosity, μ, is evaluated according to Sutherland´s equation, as a function of temperature (Anderson Jr., 1989) and ρ is the specific mass. In Eq.(4) K_1= *0.44*, K_2 = *-1* and K_3 = *1*, for laminar flow. For turbulent flow, $K_2 = K_3 = -m$, and

$$K_1 = 2\left(\frac{1}{C_5}\right)^{\frac{2N}{N+1}}\left[\frac{N}{(N+1)(N+2)}\right]^m \tag{6.a}$$

$$m = \frac{2}{N+1} \tag{6.b}$$

$$C_5 = 2.2433 + 0.93N \tag{6.c}$$

$$N = 12.76 - 6.5\log_{10}(Re_\theta) + 1.21[\log_{10}(Re_\theta)]^2 \tag{6.d}$$

For laminar flow, the boundary layer thickness is given by (Anderson Jr., 1989):

$$\theta_L = \frac{0.664\left(\int_0^y \rho_e^* \mu_e^* v_e R^2 dy'\right)^{\frac{1}{2}}}{\rho_e v_e R} \tag{7}$$

where y is measured along the body´s surface, Fig. 3.b, and $y=0$ corresponds to the stagnation region. R is a geometric parameter schematically shown in Fig. 3.b. In this work the numerical integration of Eq. (7) was obtained according to the trapezoidal method. As $R \rightarrow 0$, Eq. (7) becomes undetermined. By taking the limit of Eq. (7) as $R \rightarrow 0$, the following expression is obtained (Miranda and Mayal, 2001):

$$\theta_L = \frac{0.332\left(\rho_e^* \mu_e^*\right)^{\frac{1}{2}}}{\rho_e \sqrt{\frac{1}{R_N}\left[\frac{2(p_s - p_\infty)}{\rho_s}\right]^{\frac{1}{2}}}} \tag{8}$$

In this work Eq. (8) is applied for $y < 0.1\ R_N$, where R_N is the radius of curvature at the stagnation point.

The boundary layer thickness for turbulent flow is obtained by solving the following first order differential equation:

$$\frac{D(\rho_e v_e R\ \theta_T)}{Dy} = 0.5 C_F \rho_e v_e R \tag{9}$$

After obtaining the boundary layer momentum thickness, θ, Re_θ, C_F and h can be evaluated by using Eqs. (5), (4) and (3), respectively. Along the transition region between laminar and turbulent flow, the following relationship is used (Dhawan and Narasimha, 1958):

$$q_{Tr} = q_L + F(y)(q_T - q_L) \tag{10}$$

where the subscripts *Tr*, *L* and *T* represent, respectively, transitional, laminar and turbulent flow. The transitional factor, *F(y)*, is given by (Dhawan and Narasimha, 1958):

$$F(y) = 1 - \exp\left\{-0.412\left[\frac{4.74(y - y_L)}{(y_T - y_L)}\right]\right\} \tag{11}$$

Following (Dhawan and Narasimha, 1958) transition is supposed to occur for $163 < Re_\theta < 275$.

Properties evaluation at the boundary layer edge is performed assuming isentropic flow between the stagnation region and the location "*i*" where properties are needed, namely

$$\rho_{e,i} = \rho_s \left(\frac{p_{e,i}}{p_s}\right)^{\frac{1}{\gamma}} \tag{12.a}$$

$$h_{e,i} = h_s \left(\frac{p_{e,i}}{p_s}\right)^{\frac{\gamma-1}{\gamma}} \tag{12.b}$$

$$v_{e,i} = \sqrt{2(h_s - h_{e,i})} \tag{12.c}$$

$$T_{e,i} = \frac{h_{e,i}}{c_p} \tag{12.d}$$

The local pressure, $p_{e,i}$, is obtained from the modified Newton´s method (Anderson Jr., 1989) and $\gamma=1.4$. The subscript "*s*" appearing in Eqs. (12) refers to the stagnation condition. Eckert's reference temperature is obtained from (Anderson, 1989):

$$\frac{T^*_{e,i}}{T_{e,i}} = 1 + 0.032 M^2_{e,i} + 0.58\left(\frac{T_W}{T_{e,i}} - 1\right) \tag{13}$$

The solution procedure can be summarized as follows:

i. From a given trajectory the US Standard Atmosphere (1976) is used to obtain the free stream properties, including the stagnation ones;
ii. Normal shock relationships are used to obtain the fluid flow properties behind the shock;
iii. By using the modified Newton method, pressure distribution is obtained along the entire rocket (Machado and Villas Boas, 2006);
iv. Equations (12) provides the local properties at the boundary layer edge;
v. If $y < 0.1\ R_N$, Eq. (8) provides the laminar boundary layer thickness, leading to the estimation of Re_θ, C_F and h, provided by Eqs. (5), (4) and (3), respectively;
vi. If $y > 0.1\ R_N$ and $Re_\theta < 163$, Eq. (7) is numerically integrated up to the location where the momentum thickness is to be estimated. Such an integration is performed by using the trapezoidal method;
vii. If $y > 0.1\ R_N$ and $Re_\theta > 275$, Eq. (9) is numerically integrated by the trapezoidal rule leading to the turbulent boundary layer thickness;
viii. If $y > 0.1\ R_N$ and $163 < Re_\theta < 275$, Eqs. (10) and (11) are used to estimate h;

It should be pointed out that such a procedure is performed along the body´s surface, for different trajectory times. Therefore, $h=h(y,t)$.

2.3. Heat conduction

Once the convection heat transfer and the adiabatic wall temperature are estimated, wall temperature distributions can be obtained. The energy conservation principle is applied to an infinitesimal volume element within the wall. One-dimensional heat transfer is assumed. The physical properties of the structural and thermal protection materials are assumed to be independent on temperature. The following equation results (Özisik, 1980):

$$\rho c_P \frac{\partial T}{\partial t} = \frac{1}{R^n}\frac{\partial}{\partial R}\left(R^n k \frac{\partial T}{\partial R}\right) \tag{14}$$

The superscript *n* appearing in Eq. (14) determines the coordinates system, namely: *n = 0* for rectangular coordinates; *n=1* for cylindrical coordinates; and *n=2* for spherical coordinates. Eq. (14) is applied to several regions of the rocket, as summarized in Tab.1, that also shows the materials of which rocket parts are made, as well as their thickness, curvature radius and coordinates system. Considering the small radius of curvature of the fin leading edge (R_N= *3mm*) and its small thickness (*1 mm*), rectangular coordinates are adopted in its mathematical representation, Fig. 4. At the nose cap a spherical coordinates system is adopted and, at the payload region, Fig. 1, cylindrical coordinates are used, Fig. 5.

Table 1. Geometric Characteristics of regions studied in VSB-30.

	Region	**Material**	**Curvature radius**	**Thickness**	**Coord. System**
Fin	leading edge	stainless steel	3 mm	1 mm	rectangular
	lateral	stainless steel	-	1mm	rectangular
Nose	cap	stainless steel	10 mm	10 mm	spherical
	body and payload	aluminum	variable with *y*	6 mm	cylindrical

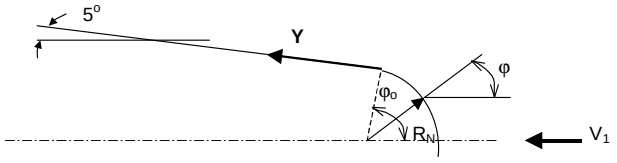

Figure 4. Coordinate system near the fin's leading edge.

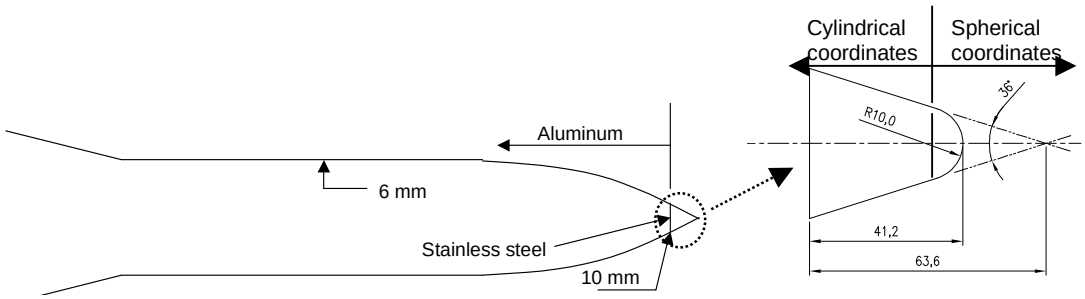

a) Payload region b) Nose cap region

Figure 5. Coordinate system at the nose and payload regions.

Since a thermal protection system is externally applied to the surfaces, the domain of calculus is divided into two different regions. Equation (14) is applied to both regions, but since the external layer corresponds to the ablative material, its thickness is variable. The internal layer is the rocket´s structure itself, which is made of metallic materials, Tab. 1. FIREX RX-2376 is applied externally to the surface. As soon as it reaches its ablative temperature, it is supposed to be removed of the surface by aerodynamic drag. Table 2 shows the physical properties of the structural and thermal protection materials used in VSB-30. The heating takes place externally, as a result of aerodynamic heating. During the time in which the surface temperature is below *138 ^oC*, called pre-ablative period, a two-layer transient one-dimensional heat conduction problem arises.

Table 2. Materials physical properties.

Property	Stainless steel (1)	Aluminum (1)	FIREX RX-2376 (2)
Specific heat	*500 J/kg K*	*960 J/kg K*	*1,674.6 J/kg K*
Thermal conductivity	*16.2 J/kg K*	*177 J/kg K*	*0.24 W/m K*
Density	*8,000 kg/m^3*	*2,710 kg/m^3*	*1,170.2 kg/m^3*
Emissivity	*0.11*	*0.06*	*1.0*(3)
Heat of ablation	-	-	*4.2 MJ/kg*
Ablative temperature	-	-	*138^o C*

(1) Özisik, 1980.
(2) Pyrogenics Group, 2003.
(3) Assumption.

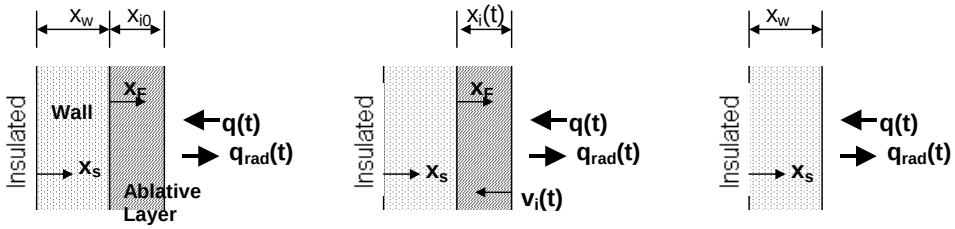

(a) Pre-ablative period (b) Ablative period (c) Pos-ablative period

Figure 6. Coordinate system for the conductive and ablative processes.

As it is depicted in Fig. 6, the internal walls are assumed insulated. At the interface structure-FIREX heat conduction takes place. From that result the following boundary conditions for the structure:

$$\left.\frac{\partial T_s}{\partial x_s}\right|_{x_s=0} = 0 \quad ; \qquad -k_s \left.\frac{\partial T_s}{\partial x_s}\right|_{x_s=x_w} = -k_F \left.\frac{\partial T_F}{\partial x_F}\right|_{x_F=0} \tag{15.a, b}$$

where subscripts *S* and *F* refer, respectively, to structure and FIREX. For the FIREX layer, three different situations may arise, Fig. 6. During the pre-ablative period, Fig.(6.a), the boundary conditions are:

$$-k_F \left.\frac{\partial T_F}{\partial x_F}\right|_{X_F=X_i} = H(t,y)\left[T_F(t,x_i) - T_{aw}\right] + \varepsilon\sigma\left[T_F^4(t,x_i) - T_\infty^4\right] \tag{16.a}$$

$$-k_s \left.\frac{\partial T_s}{\partial x_s}\right|_{x_s=x_w} = -k_F \left.\frac{\partial T_F}{\partial x_F}\right|_{x_F=0} \tag{16.b}$$

When the external surface reaches the ablation temperature:

$$T_F(t,x_i) = T_a \tag{17}$$

where T_a is the ablation temperature. Under such a condition, the ablative thickness is reduced with time, leading to the change in the physical domain. A moving coordinate system, x_{FD}, is defined and the energy conservation equation becomes (Silva, 2001):

$$x_{FD}^n \frac{\partial T_F}{\partial t} = \frac{\partial}{\partial x_{FD}}\left(\alpha_F \frac{x_{FD}^n}{x_i^2(t)}\frac{\partial T_F}{\partial x_{FD}} + \frac{v_i(t)}{x_i(t)} x_{FD}^{n+1} T_F\right) - \frac{v_i(t)}{x_i(t)}(n+1)x_{FD}^n T_F \tag{18}$$

where $x_{FD} = x_F/x_i(t)$, $x_i(t)$ and $v_i(t)$ are the position and velocity of the moving boundary, respectively. $v_i(t)$ is given by:

$$v_i(t) = \frac{H(t,y)\left[T_F(t,x_i) - T_{aw}\right] + \varepsilon\sigma\left[T_F^4(t,x_i) - T_\infty^4\right] + k_F \left.\frac{\partial T_F}{\partial x_F}\right|_{X_F=X_i}}{\rho_F L} \tag{19}$$

where L is FIREX heat of ablation, Tab. 2. Once the ablation velocity is determined, the new position of the external boundary is calculated from:

$$\frac{dx_i}{dt} = v_i \tag{20}$$

Depending on the aerodynamic heat load, the ablative layer may be totally removed of the surface and the structure may be exposed to the external flow. Under such circumstances Eq. 15.b becomes:

$$-k_s \left.\frac{\partial T_s}{\partial x_s}\right|_{X_s=X_w} = H(t,y)\left[T_s(t,x_w) - T_{aw}\right] + \varepsilon\sigma\left[T_s^4(t,x_w) - T_\infty^4\right] \tag{21}$$

The initial condition (in $t = 0$) for the whole domain is $T(x,0) = T_\infty$.

3. RESULTS

Numerical results are obtained for the temperature distributions at two different locations of VSB-30. The nose cap, including the payload region, and the second stage fin´s leading edge. The transient one-dimensional conduction-phase change material is numerically solved by the finite volume technique (Maliska, 1995). Based upon the local conditions for temperature, pressure and velocity, the convective heat transfer, *h(y,t)*, is evaluated and used to solve the energy conservation equation, from which temperature distributions are obtained. Typically 5 volumes are used to discretize the domain of calculus. The routine was implemented through a FORTRAN computer code. To run the trajectory presented in Fig. 2, for each of the locations along VSB-30 surface, about 4 hours were required in a Dell Pe IV 2800 MHz computer. Additional results from this investigation can be obtained elsewhere (Machado and Pessoa Filho, 2007)

3.1. Fins

Calculations performed on VSB-30 first stage fins showed that aerodynamic heating was not a problem. Such a result can be explained by the fact that they only work during the first 15 seconds into the flight. As a consequence, attention was focused on the second stage fins. By using the trajectory presented in Fig. 2 and the procedure outlined in section 2, the adiabatic wall temperature and the convective heat transfer coefficient were obtained at the stagnation line, Fig. 7. As in a previous work (Mazzoni et al., 2005), three different cases were considered: fin without ablative material ($x_{i0} = 0$); fin covered with *0.40 mm* of FIREX ($x_{i0} = 0.40$) and fin covered with *0.85 mm* of FIREX ($x_{i0} = 0.85$). As it is shown in Fig. 8.a, the use of FIREX had little effect on decreasing the temperature of the fin. Such a behavior is a result of the high heat flux occurring at the stagnation line, which causes the ablative material to be totally removed of the surface. According to Fig. 8.a, the layer of FIREX is totally ablated after *23* and 27 seconds into the flight. It should be pointed out that due to the high thermal diffusivity of the stainless steel, the temperature difference across its *1 mm* thickness is lower than *0.5 ^oC*. In all cases shown, the maximum temperature at the stagnation line is pretty high and close to the melting point of the stainless steel, 1,540 ^oC.

Figure 9a and Figure 9b show temperature distributions along the fin´s leading edge for *t=43 s* and *t=65 s*, corresponding to the maximum temperature at the stagnation line and the end of the atmospheric ascent flight. In Fig. 9, *y=0* corresponds to the stagnation line and *y=4 mm* corresponds to the transition between the cylindrical and flat surface of the fin´s leading edge. Once again three different cases are considered. Besides the very high temperature levels observed at the stagnation lines, for both *43* and *65* seconds into the flight, a striking factor depicted in Fig. 9 is the temperature gradient occurring along the curved surface of the leading edge. At *43 seconds*, for example, the temperature decreases from *1,450 ^oC* to less than *200 ^oC*, as we move from *y=0* to *y= 4 mm*. At 65 s, such an effect is even more pronounced with the surface temperature decreasing one order of magnitude, i.e., from *1,250 ^oC* to *150 ^oC*. As a result of such a high temperature gradient, the hypothesis of one-dimensional heat conduction across the wall thickness is no longer valid. Heat will flow in both *x* and *y* directions and, as a consequence, the temperature gradients depicted in Fig. 9, shall decrease. With regard to FIREX, the results show that its use did have an effect on decreasing the temperature of the metallic structure.

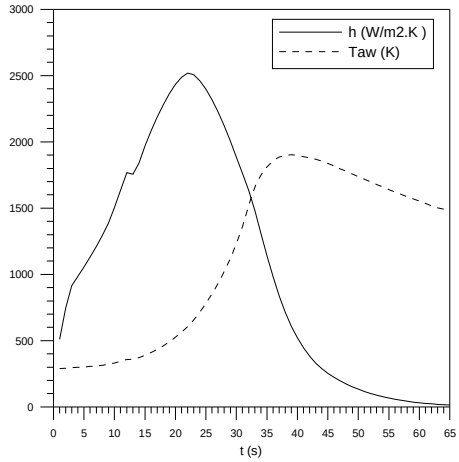

Figure 7. Convective heat transfer coefficient and adiabatic wall temperature at the fin leading edge stagnation line.

In a 2004 VSB-30 flight, temperature measurements were taken and FIREX was applied externally to the fins. The positioning of the sensors correspond to a location 10 mm away from the stagnation line, *y≈ 10 mm*. PT 100 thermo sensors were used (Fraden, 1996) and at the locations under which the sensors were installed, the FIREX layer was removed. Due to limitations of the application procedure, the thickness of FIREX applied on the fins may vary between *0.40 mm* and *0.85 mm*.

Figure 8.b shows the measured temperatures during the flight. As it is depicted in Fig. 8.b, the temperature sensors were located along the spam wise direction of the fin and large differences were observed among these measurements. They might be attributed to three-dimensional effects occurring in the real flight including, among others, rotation around the symmetry axis, in the order of *3.5 revolutions per second*. As expected, the numerical results which best fit the measurements are those obtained for the case in which FIREX is not applied to the surface.

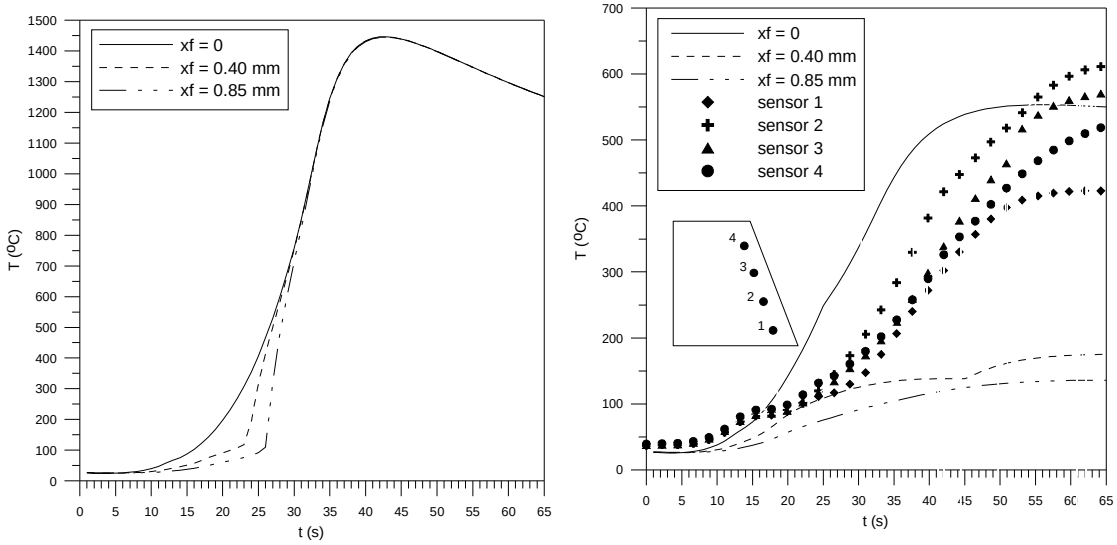

(a) At the stagnation line (b) At sensor locations

Figure 8. Temperature profiles.

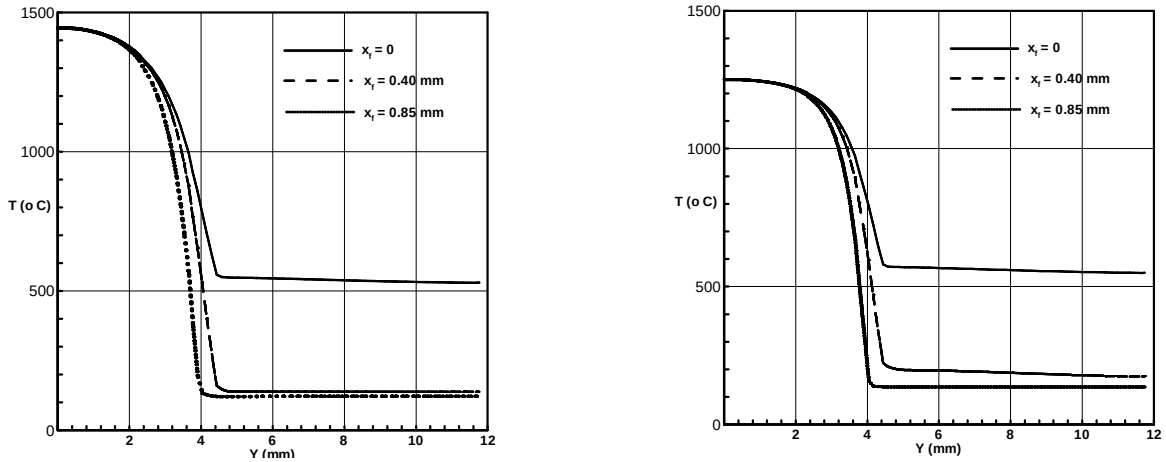

(a) t = 43 s (b) t = 65 s

Figure 9. Temperature profiles at t = 43 and 65 seconds.

3.2. Nose cap and payload

The analysis of the fin´s temperature is of utmost importance because they stabilize the rocket during its atmospheric flight. Nonetheless, special attention must be directed towards the payload region, where the microgravity experiments are housed, Fig. 1. Besides its structural integrity, it is necessary to verify the internal wall temperature. In terms of heating, the most critical region is the nose cap. Figure 10 shows h and T_{aw} evolutions at the nose cap stagnation point. Two temperature and convection heat transfer coefficient peaks are observed, one during the ascent flight, and other during payload reentry. Figure 11 shows the internal wall temperature at the nose cap, which is made of stainless steel, with a radius of curvature equal to 5 *mm*. As for the fin's stagnation line case, the temperature gets close to the stainless steel melting point, i.e., *1,540 ^oC*. The application of FIREX on this region has only a marginal effect on bringing the temperature down. In a similar fashion as in Fig. 10, two temperature peaks are observed. Between them, there is the vacuum of space and no heat is lost by convection. Nonetheless, radiative losses take place, leading to the temperature decrease shown in Fig. 11.

Figure 12.a and Fig. 12.b show the variation of the internal and external wall temperature at t=525 s, corresponding to the impact point of the payload into the ocean. Figure 12.a focuses on the spherical nose region. *y=0* corresponds to the stagnation point and *y=5 cm* corresponds to the transition between the spherical and conical geometries, Fig. 5.b. Differently from the fin´s leading edge case, the maximum temperature no longer occurs at the stagnation point, but somewhere downstream, at $y \approx 1$ *cm*. Such a behavior occurs as a result of the fact that the flow, initially laminar, becomes turbulent.

At the spherical nose region, the effects of FIREX application are noticeable leading to a temperature decrease of *200 ^oC*, approximately. It is also noticeable slight differences between the external and internal wall temperatures, around *50 ^oC*. They are due to the thickness and thermal properties of the stainless steel from which the spherical nose cap is made. Another discontinuity is verified at the transition between the spherical and conical geometry. Besides the change in geometry, there is also the change of material (aluminum) and thickness (6 *mm*), as we move from the spherical to the conical region. From that point on, there are no noticeable temperature variations across the wall, Fig. 12.b. In spite of being completely consumed after 25 and 27 seconds into the flight, the application of either 0.40 mm or 0.85 mm has an effect in decreasing the temperature by more than *100 ^oC*. In this case, the use of FIREX becomes important to assure the wall integrity during the flight, since aluminum melting temperature is about *550^o C*.

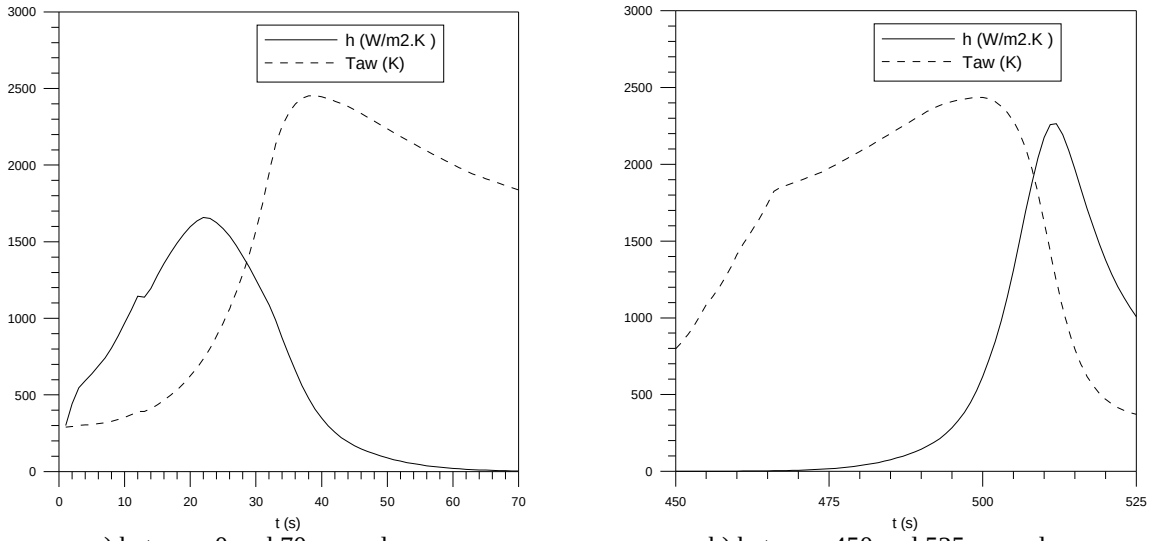

a) between 0 and 70 seconds b) between 450 and 525 seconds.

Figure 10. Convection heat transfer coefficient and adiabatic wall temperature at the stagnation point of the nose cap.

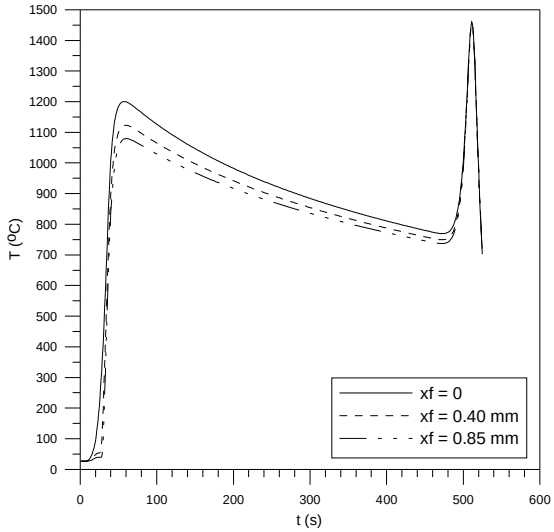

Figure 11. Internal temperature at the stagnation point of the nose cap.

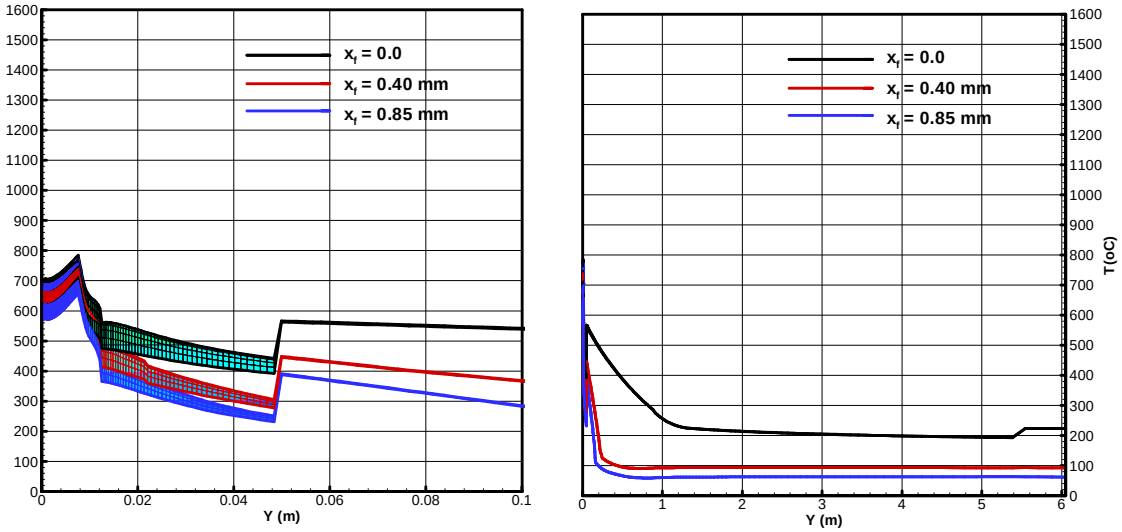

Figure 12. Payload temperature profiles at t = *525 s*.

4. CONCLUSION

Aerodynamic heating on a sounding rocket flying at hypersonic flow regime was analysed. Attention was focused ont the fin´s leading edges and the payload region. An ablative type of thermal protection system was applied on those regions and the obtained results showed it to be effective in reducing the structure's temperature. The modelling considered a transient, one-dimensional, conductive-phase change material problem. At the 2nd stage fin leading edge, it was possible to compare the predictions with measurements taken on an actual flight. By considering the approximations involved in the modeling and the uncertanties of the measurements, a fair agreement was obtained.

In a next study the modeling of a unsteady two-dimensional conduction-phase change material shall be considered. It is also intented to improve the techique for fixing the temperature sensors, as well as for applying the ablative coating. It is also intended to increase the number of measurements to be taken during the flight.

5. REFERENCES

Anderson Jr., J. D., 1989, *Hypersonic and High Temperature Gas Dynamics*, McGraw-Hill.

Anderson Jr., J. D., 1990, *Fundamentals of Aerodynamics*, McGraw-Hill.

Dhawan, S. and Narasimha, R., 1958, Some Properties of Boundary Layer Flow During the Transition from Laminar to Turbulent Motion, Journal of Fluid Mechanics, Vol. 3, Nº 4, pp. 418-436.

Fraden, J., 1996, *Handbook of Modern Sensors*, Springer, Berlin.

Garcia, A., 2003, *Cálculo da Trajetória do VSB-30*, Technical note 040-ASE, IAE/CTA.

Machado, H. A. e Villas-Boas, D. J. F., 2006, Estudo Comparativo de Modelos para Aquecimento Aerodinâmico de Veículos Espaciais, *Proceedings of ENCIT*, Curitiba.

Machado, H. A. and Pessoa Filho, J. B., 2007, Aerodynamic Heating on VSB-30, *Proceedings of 18th ESA Symposium on European Rocket and Balloon Programmes and Related Research*, Visby, Sweeden.

Maliska, C. R., 1995, *Transferência de Calor e Mecânica dos Fluidos Computacional*, LTC, Rio de Janeiro.

Mazzoni, J. A., Pessoa Filho, J. B. e Machado, H. A., 2005, Aerodynamic Heating on VSB-30 Sounding Rocket, *Proceedings of COBEM*, Ouro Preto.

Miranda, I. F. and Mayall, M. C de M., 2001, *Fluxo de Calor Convectivo em Micro-Satélites em Reentrada atmosférica*, Graduate Dissertation, ITA, Brazil.

Özisik, M. N., 1980, *Heat Conduction*, John Wiley & Sons.

Pyrogenics Group, 2003, http://www.pyrographite.com.

Silva, D. V. F. M. R., 2001, *Estimativa de propriedades Térmicas de Materiais Ablativos*, M.Sc. Dissertation, COPPE/UFRJ, Brazil.

U.S. Standard Atmosphere, 1976.

Zoby, E. V., Moss, J. N. and Sutton, K., 1981, Approximate Convective Heat Equations Hypersonic Flows, *Journal of Spacecraft and Rockets*, Vol. 18, No. 1, pp. 64-70.

6. RESPONSIBILITY NOTICE

The authors are the only responsible for the printed material included in this paper.